20XX-01-XXXX

Imaging of Fuel-Film Evaporation and Combustion in a Direct-Injection Model Experiment

Author, co-author (Do NOT enter this information. It will be pulled from participant tab in MyTechZone)

Affiliation (Do NOT enter this information. It will be pulled from participant tab in MyTechZone)

Abstract

Late-evaporating liquid fuel films within the combustion chamber are considered a major source of soot in gasoline direct-injection engines. In this study a direct-injection model experiment was developed to visualize and investigate the evaporation of fuel films and their contribution to soot formation with different diagnostic techniques. A mixture of isooctane (surrogate fuel) and toluene (fluorescent tracer) is injected by a multi-hole injector into a wind tunnel with an optically accessible test section. Air flows continuously at low speed and ambient pressure through the test section. Some of the liquid fuel impinges on the quartz-glass windows and forms fuel films. Combustion is initiated by a pair of electrodes within the fuel/air-mixture. The turbulent flame front propagates through the chamber and ignites pool fires near the fuel films, leading to locally sooting combustion. Laser-induced fluorescence (LIF) of the toluene, excited by laser pulses at 266 nm, is used to image the fuel-film thickness and to visualize the fuel vapor, while laser-induced incandescence (LII), excited at 1064 nm, is used to visualize soot. In complementary line-of-sight imaging, the natural flame luminosity, mainly from soot incandescence, is captured with a high-speed camera and schlieren imaging, combining visualization of the fuel vapor and the sooting flame. The LIF images show that the fuel films remain on the wall surface long after the flame front has passed. The evaporation rate of the individual fuel films seems to be unaffected by combustion, indicating that conductive heat transfer from the wall is the limiting factor in evaporation. The visualization of both natural flame luminosity and LII show that soot formation occurs in small regions but always close to the fuel films.

Introduction

Injecting the liquid fuel directly into the combustion chamber can provide high efficiency, performance, and knock suppression in gasoline spark-ignition engines. However, under some conditions injected fuel may wet in-cylinder surfaces, and if the fuel in these films does not evaporate and mix sufficiently with air before combustion, the resulting inhomogeneities of the fuel/air-mixture make the formation of polycyclic aromatic hydrocarbons (PAH) and soot likely. Laser diagnostics are promising tools to investigate the sub-processes in soot formation, such as spray, fuel-film formation, mixture formation, ignition, and combustion.

The correlation between fuel-films on the piston and the engine-out soot emissions was investigated by Warey et al.[1], Drake et al., Ortmann et al. [2], and Stevens et al. [3]. Warey et al. measured particulate mass and size distributions stemming from piston fuel-films for different fuels [1]. Drake et al. imaged the thickness of evaporating fuel films by refractive index matching (RIM) and identified pool fires above those by high-speed imaging of the combustion luminosity in an optically accessible DISI engine [4]. They found first soot formation from fuel rich pockets soon after the spark. However, most of this soot was oxidized in the cylinder during the remainder of the cycle. In contrast, soot formed in pool fires was not burned out due to low turbulent mixing rates and low temperatures close to the walls and was detected in some cycles until exhaust valve opening. Stojkovic et al. also revealed two distinct stages of soot formation in a direct-Injection spark-ignition (DISI) engine, operating with a stratified fuel/air-mixture, by simultaneously imaging OH* chemiluminescence (CL) and laser-induced incandescence (LII) of soot [5]. They found that early soot originates from regions close to the electrodes within regions of partially premixed combustion, indicated by OH*-CL, and is oxidized later due to high temperatures (2000 - 2400 K) and turbulent mixing. Soot formation from pool fires occurs later and becomes significant when 80% of the heat has already been released. Temperatures then are much lower (about 1700 K), such that oxidation is unlikely, leading to the persistence of soot and engine-out emissions. In a wall-guided GDI engine, Ortmann et al. visualized the formation of fuel films and their contribution to soot formation via pool fires [2]. Stevens et al. used laser-induced fluorescence (LIF) to show that for late injection, where the piston is close to the injector, significant amounts of fuel impinge on the piston [3]. High-speed imaging of the flame luminosity revealed that under these conditions pool fires may exist into the exhaust stroke because there is not enough time for film evaporation. Recently, Schulz et al. investigated the effect of rail and ambient pressure on the evaporation duration of liquid fuel films in a pressure vessel by high-speed visualization [6].

To investigate the impact of evaporating fuel films in combustion as a source of soot formation, time-resolved two-dimensional detection of the film thickness is desirable. Candidate techniques for the imaging of thin liquid films are RIM and LIF. In RIM a roughened transparent surface, such as a quartz window, is illuminated from the bottom and the backscattered light is captured with a camera. When a liquid, such as fuel, adheres to the top of the rough surface, the change in the refractive index and hence the intensity of backscattered light are smaller than when no fuel adheres to the

surface. However, at a certain thickness the technique becomes insensitive to thickness because the film covers the surface roughness and no scattered light is detected anymore [4]. Typical detectable thicknesses are in the range of 0.03 to 3 µm. Maligne and Bruneaux compared the measured fuel film-thicknesses from RIM and LIF (see below) and found them to be in a good agreement [7].

Quantitative imaging of the film thickness with LIF requires the use of a fluorescent tracer added to a liquid surrogate fuel in small concentration. By judicious choice of the tracer concentration the dynamic range of the experiment can be adjusted to the expected range of film thicknesses. Lin and Sick compared the fluorescence properties of 3-pentanone and toluene as potential tracers dissolved in iso-octane as a surrogate. They found that toluene co-evaporates better with iso-octane and has higher fluorescence quantum yield (FQY), which makes it more suitable for quantitative imaging [8]. The general applicability of LIF for liquid film-thickness imaging has already been shown in several model experiments at atmospheric pressure [9-11]. In addition, the influence of ambient pressure and temperature as well as of rail pressures and nozzle-wall distances on the liquid film formation were investigated by Schulz et al. via LIF [12, 13]. Zheng et al. and Senda et al. investigated the effect of injection duration and impingement angle on the fuel-film thickness, area, and mass by RIM and LIF on flat surfaces, and compared the results to simulations [14, 15]. Pointwise LIF measurements of fuel film-thickness were carried out by Cheng et al. under a variety of process parameters [16]. Other studies performed pointwise measurements of the fuel-film thickness in the intake or combustion chamber of metal engines [17, 18]. Park et al. conducted simultaneous single-point measurements of fuel-film temperature and thickness in a DISI engine by means of LIF [19]. The LIF-based temperature measurement exploited the red-shift of the fluorescence spectrum with increasing temperature. They found that the film temperature follows the piston temperature quite well during the cycle. Quantitative LIF fuel-film imaging on the piston window of an optical DISI engine was recently performed by Geiler et al. [20]. An important outcome was that, when performing LIF fuel-film imaging, the interfering LIF signal from the gas phase is suppressed by quenching by oxygen.

As the fuel films evaporate, inhomogeneities in the fuel/air-mixture arise near the films. The visualization of the nearby gaseous fuel is desirable, since soot formation is most likely in these regions. Tracer LIF in the gas phase is much more common than in the liquid phase, and overviews of the technique can be found in [21] and comparisons of the photophyiscal properties of selected tracers in [22, 23]. When pressure and temperature vary, quantitative LIF imaging becomes more difficult due to the dependencies of the LIF signal on these parameters. In isobaric and isothermal systems, tracer LIF of a gaseous flow gives information about local fuel concentrations [21]. A qualitative visualization of the fuel/air-mixing above evaporating fuel films was carried out by Alger et al. in an optical DISI engine [24]. Schlieren imaging, as a qualitative line-of-sight imaging technique, also visualizes the flow of gaseous fuel. Montanaro et al. visualized both the liquid and gaseous fuel during spray-wall interaction in a quiescent chamber for different wall temperatures by schlieren and Mie-scatter imaging [25, 26].

When the premixed flame front reaches the inhomogeneous fuel/air-mixture near the fuel films, it may turn to a non-premixed flame, producing soot. Laser-induced incandescence and high-speed combustion-imaging are sophisticated techniques for the visualization of soot. Notably, Dec et al. investigated the soot formation in Diesel engines with LII imaging [27, 28] and developed a conceptual model of the different combustion stages [29]. In DISI engines, the formation of soot from diffusion flames, in particular from pool fires, has barely been investigated. By means of LII, two-dimensional imaging of soot volume fraction [30] and particle size [31] were performed in GDI engines. When fuel films persist into the exhaust stroke and the local temperature is too low to cause soot formation, unburned hydrocarbons are emitted [24, 32-34].

Previous studies mostly image either the thickness of evaporating fuel-films or the formation of soot. When both phenomena are investigated, soot formation is mostly visualized by line-of-sight imaging of the combustion luminosity, making the correlation to the fuel-film's evaporation characteristics difficult. Here, we image both the fuel-film evaporation and the formation of soot from these films in combustion. First, we used LIF to image the film thickness and quantitatively investigate evaporation with and without combustion. Second, we used laser-light-sheet diagnostics, LIF and LII, to image relative fuel and soot concentrations in a plane intersecting the fuel films. Complementary to that, schlieren imaging and high-speed combustion-imaging were used to visualize fuel-film evaporation and soot along the line-of-sight. Thus, this study investigates the relation between evaporating fuel films and the spatial and temporal formation of soot nearby.

Experiment

Flow facility

A sketch of the DISI model experiment, the optically accessible test section of a wind tunnel, is shown in Figure 1.

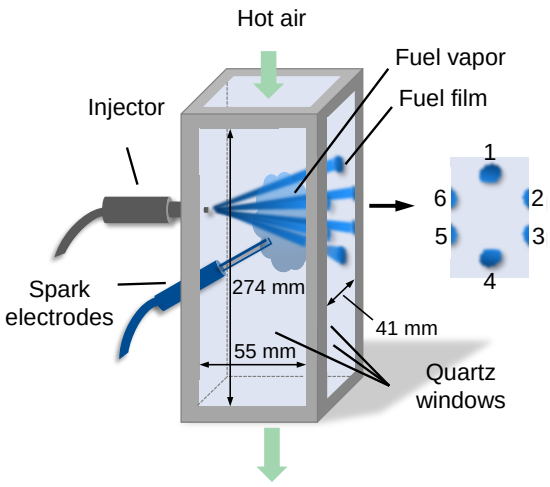

Figure 1: (left) Optically accessible test section of wind tunnel with injector and spark electrodes. (right) Numbering of the six fuel films.

The test section of our tunnel consists of three quartz walls that provide optical access. An injector and spark electrodes protrude through an aluminum plate, the fourth wall of the section. Heated air flows continuously from the top to bottom with a nominal velocity of 2.23 m/s. A perforated plate stacked with fine wire meshing is located between the air heater and the test section to provide small-scale turbulence and a uniform bulk flow. A six-hole injector injects fuel evaporating into the hot air flow. Some of the injected fuel wets the quartz wall on the opposite side. Fuel films 1 (topmost) and 4 (bottommost) lie completely on the quartz wall, as indicated in Figure

1. The remaining four spray cones impinge mainly on the metal frame next to the quartz window. Thus, fuel films 2, 3, 5, and 6 lie only to small extent on the quartz wall The impingement distance (the distance between the nozzle tip and the wall) is approximately 45 mm. Ignition of the fuel/air-mixture is performed by the electrodes below the injector, acting as a spark plug, (see Fig. 1) 1 ms after the end of the injection. Therefore, the experiment employs a combination of a spray-guided and wall-guided direct-injection strategy. The latter is known to potentially lead to increased soot formation [35].

Table 1 gives an overview of the operating conditions in the experiments. Parameters that were varied in the experiments are the air temperature and the injection duration (and thus the injected mass). The air, wall, and injector temperature cannot be controlled independently but follow the air temperature as given in Table 1. The injected mass increased linearly with increasing injection duration. A minimum injection duration of 1 ms was required to trigger the injector.

Table 1: Operating conditions.

Fuel	Iso-octane + 1%/ 10% toluene
Injector	Six holes
Rail pressure	100 bar
Injector temperature	360 K (325 K, 340 K)
Injection duration	2.1 ms (14 mg), 2.6 ms (21 mg)
Nominal flow rate	13 g/s
Air temperature	381 K (340 K, 361 K)
Air flow velocity	2.23 m/s
Back pressure	1 bar
Quartz wall temperature	365 K (330 K, 345 K)

Figure 2 (left) shows a view through the front quartz window into the test section with injector tip and spark plug. After preliminary experiments, a conventional spark plug was replaced by two thin electrodes, as shown in Figure 2, disturbing the flow and obscuring the view less.

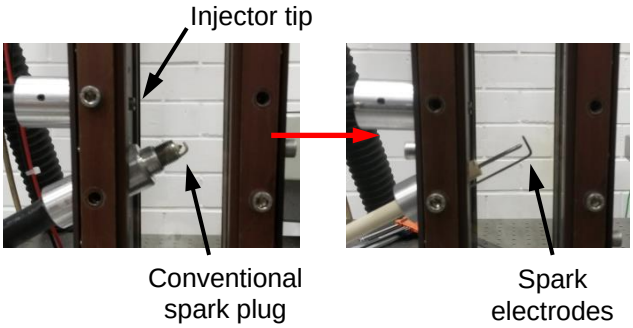

Figure 2: Conventional engine spark plug and custom spark electrodes in the wind tunnel.

LIF for liquid-film imaging

The absorption of light is described by the Beer-Lambert law [36],

$$I_t = I_0 \cdot e^{-(\varepsilon^* \cdot c \cdot d)}. \quad (1)$$

Here I_t denotes the transmitted intensity, I_0 the incident intensity, ε^* the molar extinction coefficient, c the molar concentration of the absorbing species, and d the absorption path length. Therefore, the "absorbed intensity" I_a is equal to the difference between incident and transmitted intensity:

$$I_a = I_0 \cdot (1 - e^{-(\varepsilon^* \cdot c \cdot d)}) \quad (2)$$

The absorption of light by a molecule can promote an electron from the ground level to a higher energy level. In the conditions considered here, within that excited electronic state the molecule quickly relaxes to vibrational and rotational equilibrium. When the electron returns to the ground state, the remaining energy is released by the emission of a photon, a process known as a fluorescence [37].

The detected fluorescence intensity is proportional to the absorbed intensity, the FQY $\phi \left(\frac{\#\ photons\ emitted}{\#\ photons\ absorbed}\right)$, and the collection and detection efficiency $\Omega \cdot \eta$ of the imaging system [15]:

$$I_f = \phi \cdot \Omega \cdot \eta \cdot I_a \quad (3)$$

Combining Equations (2) and (3), the fluorescence intensity is given by

$$I_f = \phi \cdot \Omega \cdot \eta \cdot I_0 \cdot (1 - e^{-(\varepsilon^* \cdot c \cdot d)}). \quad (4)$$

When the exponent in Equation (4) is small, the fluorescence intensity is in good approximation proportional to the concentration of the fluorescing species and the absorption path length, the latter being the desired quantity in liquid-film imaging:

$$I_f = \phi \cdot \Omega \cdot \eta \cdot I_0 \cdot \varepsilon^* \cdot c \cdot d \quad (5)$$

Optical setup

Fuel-film imaging

The experiment for fuel-film imaging is shown in Figure 3. A Pellin-Broca prism separated the fourth harmonic (266 nm) from an Nd:YAG laser (Litron Nano L PIV Series) from the remaining second harmonic (532 nm). The pulse energy was adjusted by a dielectric beam attenuator. A quartz wedge reflected some portion of the laser light to an energy monitor to account for shot-to-shot fluctuations in energy. Two UV mirrors deflected the beam towards the test section. A negative spherical lens (f = -100 mm) and a negative cylindrical lens (f = -120 mm) expanded the beam vertically and horizontally. An aperture clipped the UV laser so that only the region of interest of the quartz wall was illuminated. The fluorescence was imaged by a UV lens (f = 90 mm, f/4.5) on an intensified CCD camera (LaVision), indicated by the dashed lines in Figure 3. A long-pass filter, LP 266 (Semrock 266 nm RazorEdge), blocked laser stray light and a bandpass filter, BP 292/27 (Semrock 292/27 BrightLine HC), spectrally further narrowed the detection region to suppress background fluorescence from the aluminum back

plate of the wind tunnel, the injector tip, and the electrodes. The projected pixel size was 0.11 mm/pixel. The time between two images was long enough to entirely evaporate the fuel film and flush the fuel vapor from the test section, such that each image shows an individual injection at a certain time after start of injection (aSOI).

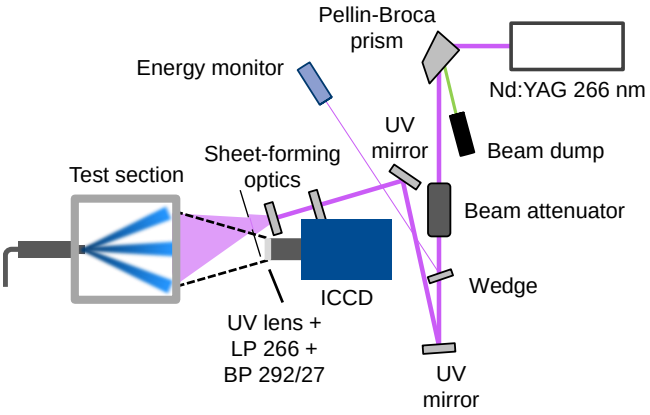

Figure 3: Optical layout for fuel-film LIF.

Fuel-vapor and soot imaging

Figure 4 shows a plan view of the experiment for fuel vapor and soot imaging. Here, the laser sheet formed a two dimensional plane within the wind tunnel at 266 nm for fuel-vapor LIF or 1064 nm for soot LII. Again, the beam was deflected towards the wind tunnel by the Pellin-Broca prism and mirrors. A positive cylindrical lens (f = 400 mm) focused the laser beam horizontally. A negative cylindrical lens (f = -25 mm) expanded the beam vertically to a light sheet.

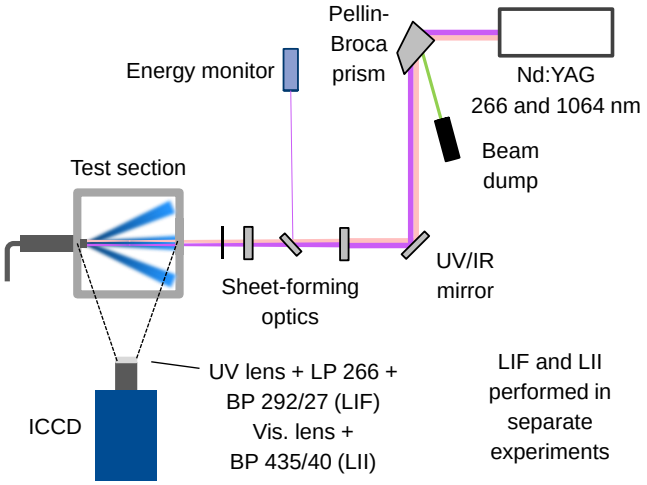

Figure 4: Optical layout for fuel-vapor LIF and soot LII.

An aperture clipped the light sheet vertically. Horizontally, the sheet had a slight offset relatively to the center plane of the test section to avoid shadowing by the electrodes. For LIF, the intensified CCD camera was equipped with a UV-lens (Cerco, f = 45 mm, f/1.8) and the same filter combination as for the fuel-film imaging. For LII, the camera was equipped with a lens for detection of visible light (Nikon, f = 50 mm, f/1.8) and a bandpass filter, BP 435/40 (Semrock 435/40 BrightLine HC). The laser fluence was kept below 0.5 J/cm² to avoid interference from C2 Swan-bands and C3 Swings-bands [38]. The projected pixel size was 0.15 mm/pixel. Again, the time between two images was long enough to flush the fuel vapor from the test section. In the current work, LIF and LII imaging were performed in separate experiments.

Tracer

Commercial fuels contain many different components that fluoresce when excited by UV lasers. Every component has different photophysical properties, meaning that the LIF signal of each component depends on temperature, pressure, and bath gas composition. Therefore, it is very difficult to derive quantitative information, such as species concentration, from the total detected signal, which is the sum of the individual contributions. For quantitative LIF imaging of fuels, a mixture of a fluorescent marker and a non-fluorescing surrogate is usually chosen [21]. In this work iso-octane (boiling point: 372 K) was chosen as the non-fluorescing surrogate, and toluene (boiling point: 384 K) as the fluorescent tracer. Figure 5 shows the fluorescence spectrum of toluene dissolved in liquid cyclohexane and upon excitation at 266 nm [39]. Also, the transmission of the LP 266, blocking laser stray light, and BP 292/27, isolating the toluene fluorescence from background fluorescence, are shown [40, 41].

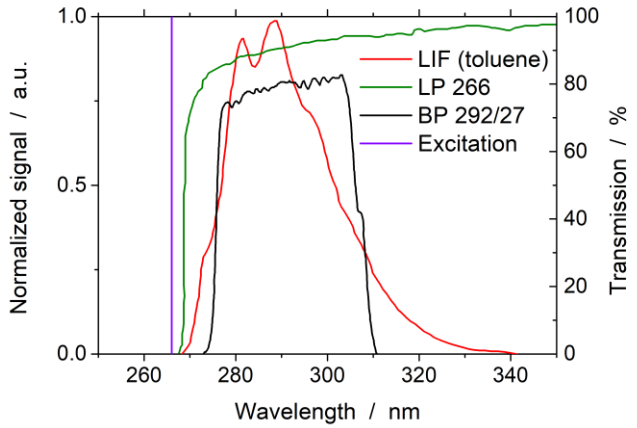

Figure 5: Fluorescence spectrum of liquid toluene, excited at 266 nm [39], and transmission of filters used for LIF (toluene) [40, 41].

The tracer should co-evaporate with the surrogate and exhibit similar properties in terms of viscosity, diffusivity, and surface tension [21]. For fuel-film imaging, it is particularly important that the surrogate fuel and the tracer co-evaporate so that the mixture fraction of the tracer is similar in liquid and gaseous fuel. Also, the spectral properties of the tracer, the dependence of the LIF signal on temperature, pressure, and bath-gas composition need to be known for quantitative measurements [42]. Toluene mostly fulfills these requirements. For LIF imaging, the volume fraction of toluene in iso-octane was 1 vol.-%. Since the tracer number density was about 2500 times lower in the gas phase and quenching by oxygen also leads to strong signal decrease in fuel-vapor imaging, here the tracer volume fraction was 10 vol.-%.

Line-of-sight imaging

As complementary techniques, high-speed line-of-sight imaging of the natural flame luminosity, mainly from soot incandescence, and schlieren imaging of both film evaporation and flame luminosity

were used. The experimental arrangement for schlieren imaging is shown in Figure 6. For schlieren imaging a blue LED (pulse width 5 µs) was used as a light source. To achieve a point-like light source and generate highly collimated light behind the collimator lens (f = 500 mm), an aperture clipped the image of the LED, produced by a condensing lens (f = 50 mm), by 40 % to 0.7 mm in diameter. A mirror redirected the light towards the test section and the beam was focused by a second lens (f = 500 mm) onto a round aperture. A high-speed camera (Phantom V7.3) with a makro lens (Nikon, f = 105 mm, f/2.8) was exposed for 10 µs at 5000 frames per second.

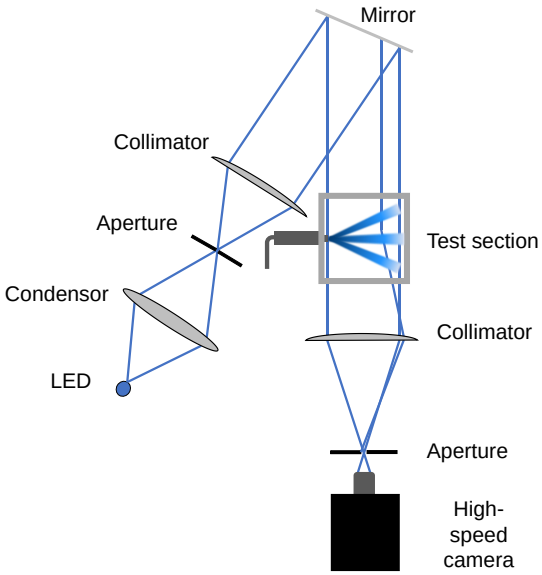

Figure 6: Experimental setup for schlieren and high-speed combustion-imaging.

In combustion imaging, the optics for schlieren imaging, shown in Figure 6, were removed. The high-speed camera (Phantom V7.3) was equipped with a shorter lens (Nikon, f = 50 mm, f/1.8) and an orange-glass filter (Schott, OG550, d = 3 mm) to transmit mainly soot incandescence. The camera was focused on the center plane of the test section and operated with an exposure of 50 µs at 6700 frames per second.

Flat-field and calibration

Fuel-film imaging

To account for the spatially inhomogeneous excitation, detection, and collection efficiencies in fuel-film LIF imaging, a sample was illuminated giving a uniform LIF response to laser excitation. Such a "flat-field" was acquired for the fuel-film imaging by illuminating a plate of quartz glass of inferior quality, which fluoresced homogeneously when excited at 266 nm. The flat-field plate was located behind the quartz wall, as indicated in Figure 7. The left image in the bottom of Figure 7, Flat-field (a), shows the LIF signal of the quartz plate when the laser light partially passes through the plate and is reflected at the aluminum back wall, where injector and electrodes were mounted. We used this flat-field to correct the fuel-film images. Since in the calibration images with a thin-film cuvette, as discussed below, these reflections do not occur, flat-field (b) was acquired with a black background and was used to correct the calibration images.

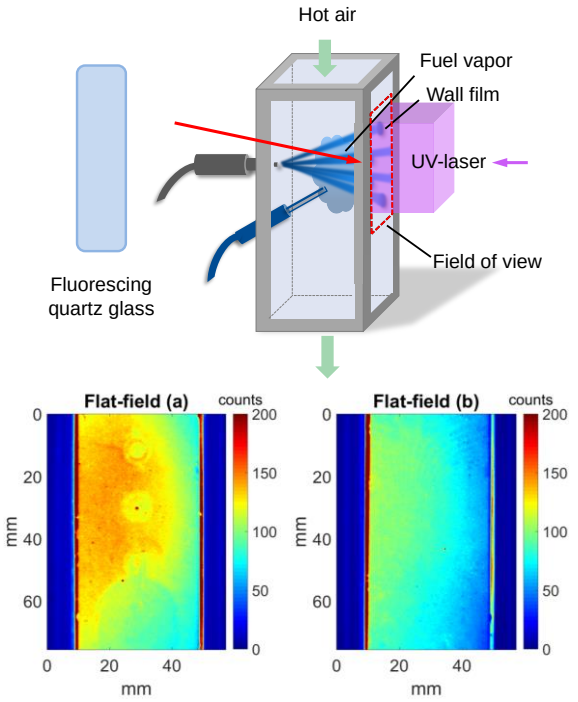

Figure 7: (top) Flat-field imaging for fuel-film LIF. (bottom) Flat-fields for (left) fuel films and (right) calibration

Fuel films with a range of thicknesses were generated in a calibration tool. Thin precision shims created a gap of known distance between a black back wall and a quartz plate of the calibration tool shown in the top left in Figure 8.

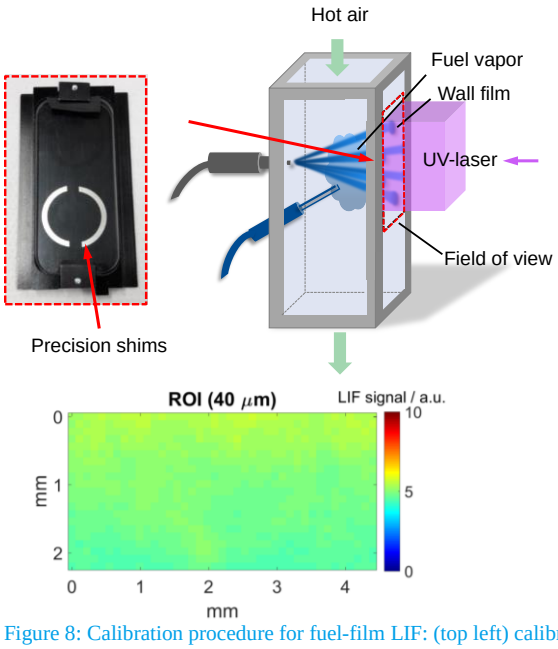

Figure 8: Calibration procedure for fuel-film LIF: (top left) calibration tool, (top right) in-situ illumination of tool, (bottom) resulting image for a thickness of 40 µm after flat-field correction.

The gap was filled with the iso-octane/toluene mixture. The calibration tool was mounted just behind the quartz-wall, to perform an in-situ calibration with excitation, collection, and detection efficiencies locally equal to those in flat-field and fuel-film imaging. The bottom image shows the detected LIF intensity from a fuel layer with 40 µm thickness after flat-field correction. The spatial standard deviation in the corrected image was 6%.

Figure 9 shows the resulting calibration function for LIF intensities with shim thicknesses ranging from 20 to 100 µm. Each data point is the average of three individual measurements, each comprising the ensemble average of 100 background- and flat-field corrected single shots. From this ensemble average, the spatial mean in a region between the two shims was calculated. In Figure 9 the deviation from the linear approximation between the LIF signal and the fuel-film thickness (Equation 5) becomes pronounced at around 100 µm. The fit-function "Beer Lambert-law" is based on Equation (4) with the factor $(\phi \cdot \Omega \cdot \eta \cdot I_0)$ and the extinction coefficient ε^* as fit parameters according to the following equation:

$$I_{\mathrm{f,cal}} = A \cdot (1 - e^{-(\varepsilon^* \cdot c \cdot d)}) \qquad (6)$$

The product $(\phi \cdot \Omega \cdot \eta \cdot I_0)$ is denoted A and represents the LIF signal of an infinitely thick fuel film. $I_{f,cal}$ is the background and flat-field corrected LIF intensity at a certain thickness d. From the fit A is 17.78 and ε^* 75.6 dm³/(cm*mol). Ramart-Lucas and Bertucat found a value for the molar extinction coefficient of 108 dm³/(cm*mol) for pure toluene [43], Lin and Sick of 122 dm³/(cm*mol) for toluene in iso-octane [8], and Berlman of 170 dm³/(cm*mol) for toluene in cyclohexane [39]. In a separate direct absorption measurement the extinction coefficient at 266 nm was measured as 170 dm³/(cm*mol). This result is equal to the one from Berlman. The inaccuracy in determining ε^* from the calibration function stems from the fact that both A and ε^* are unknown. One would need to know the saturation LIF intensity A to determine ε^* in a more accurate way. However, the fit approximates the data points very well, indicated by a coefficient of determination of 99.8%, and is used to calibrate the fuel-film images.

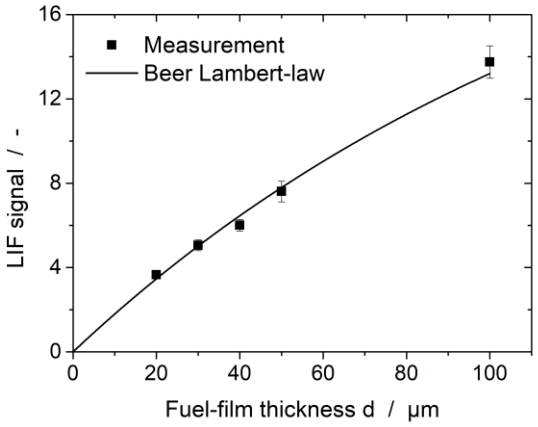

Figure 9: Calibration data of LIF signal versus fuel-film thickness. Error bars indicate the standard deviation in three individual measurements.

For processing the images, each single shot was background- and flat-field corrected. With the calibration constant $\frac{d_{\mathrm{cal}}}{I_{\mathrm{f,cal}}}$ the fuel film thickness was calculated pixel-wise according to:

$$d_{\mathrm{Film}}(x,y) = \frac{I_{\mathrm{f,exp}}(x,y)}{I_{\mathrm{f,cal}}} \cdot d_{\mathrm{cal}} \cdot \frac{E_{\mathrm{Reference}}}{E_{\mathrm{Measured}}} \cdot \frac{I_{\mathrm{f}}(298\ K)}{I_{\mathrm{f}}(T_{\mathrm{Wall}})} \qquad (7)$$

The background and flat-field corrected fluorescence intensity of the fuel films is $I_{\mathrm{f,exp}}$, while the one in the calibration is denoted as $I_{\mathrm{f,cal}}$. The ratio $\frac{d_{\mathrm{cal}}}{I_{\mathrm{f,cal}}}$ results from the calibration function. The correction of shot-to-shot fluctuations in laser energy was accounted for by $\frac{E_{\mathrm{reference}}}{E_{\mathrm{measured}}}$. The fuel film temperature was approximated as the quartz-wall temperature. The temperature of the injector tip, which was assumed to represent the initial fuel temperature, was about 5 K lower than the wall temperature. This would lead to a slight overprediction (maximum 9%) of the film mass at 3 ms aSOI, if the fuel had not reached the wall temperature yet. Once the fuel adheres to the wall it approaches the quartz wall's temperature. Park et al. stated that the fuel film temperature is similar to the piston temperature [19]. Therefore, the acquired image was corrected by the ratio $\frac{I_{\mathrm{f}}(298\ K)}{I_{\mathrm{f}}(T_{Wall})}$, where $I_{\mathrm{f}}(298\ K)$ is the LIF signal at 298 K, and $I_f(T_{\mathrm{Wall}})$ that at quartz-wall temperature. The required temperature dependence of the LIF signal of liquid toluene was taken from Geiler et al. [20]. A deviation of the liquid film's temperature of 10 K relatively to the wall temperature would result in an error of 18% in the measured film thickness.

Precision and accuracy

The relative standard deviation between the calibration measurements for each film-thickness is about 5%. For the calibration with 100 µm, the signal-to-noise ratio (SNR) is 17, indicating a spatial standard deviation of 5.8%. Assuming that the noise is shot noise dominated, the signal-to-noise ratio becomes 5.3 for 10 µm thickness films, indicating a noise of 18.6% as a maximum precision uncertainty. Thus, the total precision uncertainty is between 7.6 and 19.2%. A micrometer screw was used to determine the thickness of the distance shims used for calibration. The manufacturer states its inaccuracy with +/- 1 µm. This results in a maximum inaccuracy of 5% when calibrating with 20 µm shims. A maximum inaccuracy of about 9% in the predicted film thickness is possible because of the temperature difference between the injector and the quartz wall of 5 K. If we assume the fuel film to quickly reach wall temperature, this error becomes negligible soon after aSOI. Therefore, the total inaccuracy is 10.3%.

Fuel-vapor imaging

Calibration of the fuel-vapor mole fraction versus the LIF signal and acquisition of a corresponding flat-field were done with the same arrangement. The air flow through the wind tunnel was interrupted by inserting metal sheets into the top and bottom of the optically accessible section, as indicated on the left in Figure 10. A known mass of fuel was injected into the resulting closed volume and evaporated. A small fan in the lower part of the section increased the mixing of air and fuel vapor. Evaporative cooling of the mixture due to the fuel injection was neglected because of small temperature changes in calculating the state of the resulting gaseous mixture. However, the increase in total pressure and thus density due to the injected fuel was considered. In the example image in Figure 10 the mole fraction of fuel is 2.7%. The laser sheet enters from the right. The dashed red line indicates the back edge of the quartz wall. The black arrows indicate the height of the fuel films 1 and 4 relatively to the injector. The LIF intensity decreases towards the upper and lower

outsides of the image mainly because of the transverse intensity profile of the laser. Also, the field-dependent collection and detection efficiencies of the imaging system cause intensity gradients.

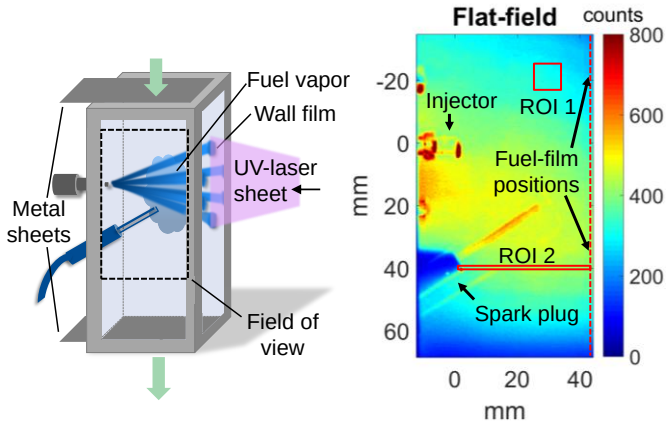

Figure 10: Calibration and flat-field setup: (left) covering top and bottom of wind tunnel with metal sheets to generate a closed volume, (right) ensemble average of 100 single shots after 15 injections into the volume.

The injector tip is at the origin of the coordinate system. The electrodes were slightly behind the illumination plane, but they blocked a small part of the laser sheet in the lower part of the image. High signal at the injector tip indicates leakage. The high intensities close to the left wall stem from diffuse back reflections of the laser sheet and fluorescence from the nozzle and bolts above and below the nozzle.

For calibrating the LIF signal versus the fuel-vapor mole-fraction, the spatial mean of the LIF signal in a region of interest (ROI 1) was calculated for different mole fractions. Figure 11 shows the resulting calibration function. Since the formation of soot close to the fuel-films is of interest, the ROI is chosen close to fuel film 1. The coefficient of determination of the linear fit is 99%, indicating a very good approximation to the data points by the fit.

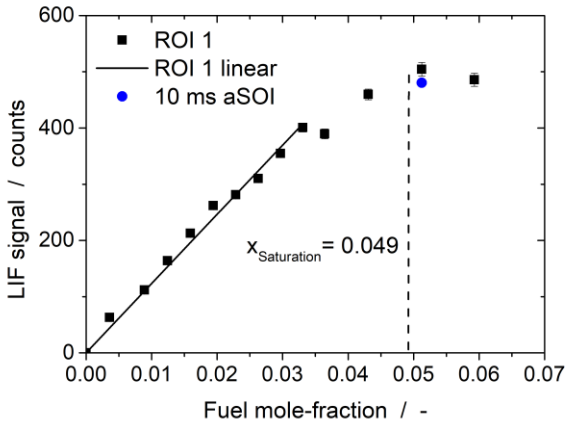

Figure 11: Calibration data of LIF signal versus fuel-vapor mole-fraction. Error bars indicate the standard deviation of the signal from 100 single shots.

Around a mole fraction of 3.5% the measured LIF signal does not follow the linear trend anymore. This is due to the fact that the saturation concentration of 4.9% (calculated from Dalton's law) is approached and evaporation becomes slower. Therefore, the time between fuel injection and image acquisition was too short to evaporate the entire injected fuel. The LIF signal saturated at a mole fraction of about 5 %, as expected. To check for excessive absorption of the exciting laser sheet when passing through the fuel films on the quartz wall, an image was acquired during film evaporation 10 ms after start of injection at a mole fraction of 6%, see Figure 11. Significant absorption of the laser by the liquid would have led to a clearly lower LIF signal at that mole fraction than without the liquid on the wall. The LIF signal was only 4% lower at 10 ms aSOI than the signal without a fuel film.

In a next step it was clarified that the non-linear relation between the LIF signal and the fuel concentration in Figure 11 do not stem from laser absorption in the gas phase. Therefore, LIF signal was vertically integrated in ROI 2, indicated in the lower part of the image in Figure 10 for the maximum investigated mole fraction of nominally 6.3 %. The result is a clearly linear relation of the signal with increasing distance from right to left (graph not shown here). This linear relationship over 4 cm path length can be expected. The 700 times lower density and the dilution with air in the test section lead to a 2500 times lower concentration of toluene in the fuel vapor than in the liquid fuel. Therefore, the absorption of the laser in a 4 cm thick fuel-vapor layer equals that in 16 µm of liquid fuel film.

The image processing of the fuel-vapor images is similar to that in fuel-film imaging. A background correction was applied to each acquired image. Pixel-wise multiplication of the corrected image with the fuel-vapor mole-fraction, according to Equation 8, results in the calibrated image:

$$x_{\mathrm{Fuel}}(x,y) = \frac{I_{\mathrm{f,exp}}(x,y)}{I_{\mathrm{f,FF}}} \cdot x_{\mathrm{fuel,FF}} \cdot \frac{E_{\mathrm{Reference}}}{E_{\mathrm{Measured}}} \cdot \frac{I_f(298\ K)}{I_f(T_{\mathrm{Air}})} \qquad (8)$$

Here, $I_{\mathrm{f,exp}}(x,y)$ is the background corrected LIF intensity during the measurement and $I_{\mathrm{f,FF}}$ the background corrected flat-field intensity, which belongs to the known fuel-vapor mole-fraction $x_{\mathrm{fuel,FF}}$. The difference in temperature of the toluene vapor in the calibration and in the measurement was taken into account by the ratio $\frac{I_f(298\ K)}{I_f(T_{\mathrm{Air}})}$, where $I_f(298\ K)$ is the LIF signal of gaseous toluene at 298 K, and $I_f(T_{\mathrm{Air}})$ that of gaseous toluene at air temperature. It was assumed that the toluene vapor is at the same temperature as the incoming air. The LIF signal of gaseous toluene in air is relatively insensitive to temperature. Within a temperature range from 365 K (wall temperature) to 381 K (incoming air temperature), the LIF signal of the toluene vapor increases about 5% [44]. Therefore, the error from temperature fluctuations throughout the field of view is small. The insensitivity against temperature variations originates from strong quenching by oxygen, the dominating depopulation mechanism of the excited state at these temperatures. The effect of oxygen quenching was considered to be equal in flat-field and actual measurement since both were acquired at an oxygen partial pressure of about 0.21 bar. If the partial pressure was different in flat-field and measurement, the FQY would be different too, requiring a further correction term in Equation (8).

Precision and accuracy

The maximum precision uncertainty is 10.4% in the calibration for the lowest mole fraction of 0.4%. Inaccuracies in determining the fuel-vapor mole-fraction mainly stem from temperature fluctuations. The maximum temperature difference between air and fuel vapor is 26 K (minimum fuel-vapor temperature is the wall temperature)

resulting in a maximum inaccuracy of 7.6% in the fuel-vapor mole-fraction determination.

Results

Fuel films

Figure 12 (a) shows the thickness of the six fuel films 3 ms after start of injection as an ensemble average of 30 single injections. Four out of the six films (films 2, 3, 5, and 6) do not lie completely on the quartz wall. They adhere mostly to the metal frame around the quartz wall.

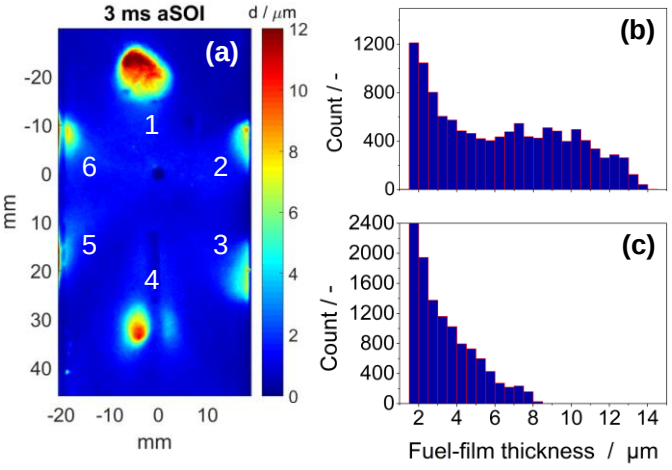

Figure 12: (a) Fuel-film formation on the quartz window 3 ms after start of injection and thickness histograms of fuel films (b) 1 and (c) 4.

In the origin of the image is the injector tip. One of the electrodes can be seen below the injector, between 11 and 45 mm. The collision of the lower spray cone with the electrodes leads to the double-lobed shape of fuel film 4. Because of this, and because of the longer spray cone penetration through the wind tunnel, this fuel-film is on average thinner than the one in the top (film 1), also indicated by the histograms in Figure 12 (b) and (c). The median is 3 µm for film 4 and 6 µm for film 1. The maximum detected ensemble-average film-thickness is 8.5 µm for film 4 and 14 µm for film 1.

Figure 13 shows the temporal evolution of ensemble averages (top) and single shots (bottom) of the evaporating film 1 with combustion, i.e. after the fuel/air mixture has been ignited by the electrodes in the test section. The propagation of the turbulent flame front through the mixture happens between 3 and 20 ms aSOI. The wall temperature is 365 K in this case. The injection duration is 2.1 ms (14 mg). The impingement angle (the angle between the spray cone axis and the wall) is approximately 65°. The distance from the injector to the wall is about 45 mm. Thus, the impingement distance is 50 mm. Results of the fuel-film evaporation without combustion, for longer injection duration, and for a different impingement angle and distance will be presented later in this section. The central row indicates the thickness along the dashed line, shown in the ensemble average at 3 ms aSOI. The images at 3, 25, 75, and 100 ms aSOI are ensemble averages of 30 single shots while the ones at 10 and 50 ms aSOI are averages of 70 single shots.

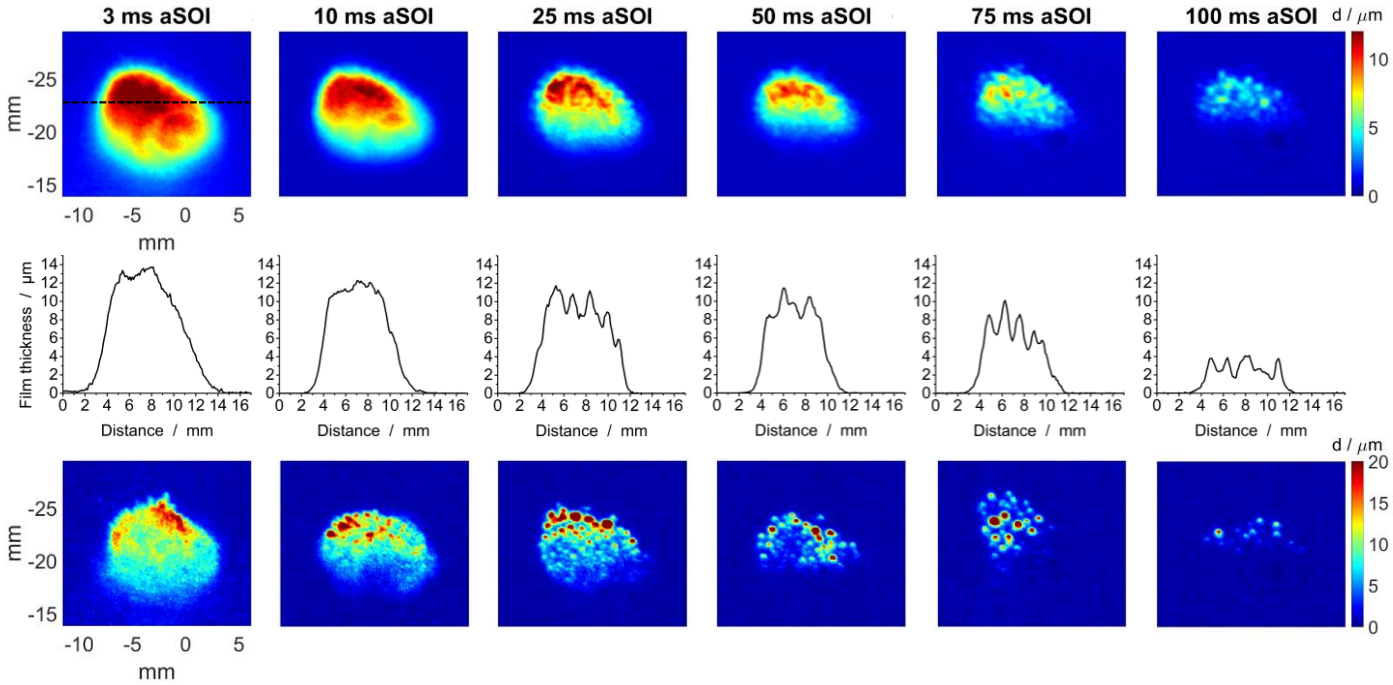

Figure 13: Film evaporation: (top) Ensemble average images of the thickness of film 1. (center) Film thickness along dashed line. (bottom) Single shots of the thickness of film 1.

The momentum of the spray cone in the vertical direction results in an accumulation of fuel in the outer part of the wetted area. Previous studies also found that the fuel film is thin in the spray impact area and accumulates toward the film tip [13, 14, 20]. At 3 ms aSOI some very thin regions, with thicknesses between 2 and 4 µm, are apparent in the periphery of the film. These thin regions have evaporated by 10 ms aSOI and a clear boundary of the fuel film becomes visible. Combustion of the fuel/air mixture is initiated 3 ms aSOI. Both the film's area and thickness decrease in time due to evaporation. The single shots show that fuel accumulates in small regions at 50 ms aSOI and later times, leading to the formation of discrete fuel "blobs" or droplets. Also Schulz et al. observed the contraction of the fuel film in some regions into such small, thick droplets [12]. The fuel film has almost completely evaporated at 100 ms aSOI.

Figure 14 shows ensemble averages of fuel film 4, showing the evaporation from 3 to 50 ms aSOI. The images were acquired with combustion for an injection duration of 2.1 ms. The wall temperature was 365 K. In contrast to film 1 the impingement angle between the spray cone and the wall is 50° and the impingement distance 60 mm for film 4. The double-lobed shape, caused by the electrodes in the spray path, was already discussed above.

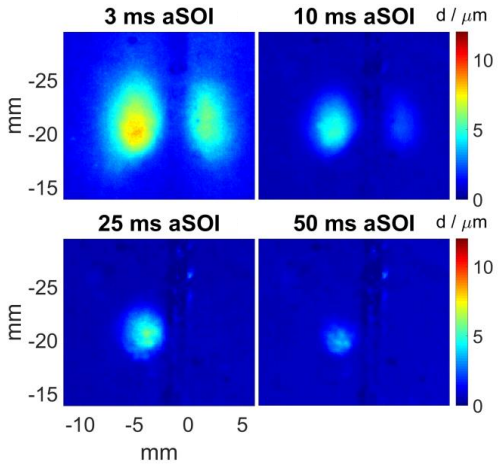

Figure 14: Film evaporation: Ensemble average images of thickness of fuel film 4.

For the calculation of the total film area and volume the thickness images were thresholded at 1.5 µm in film thickness. Pixel-wise multiplication of the film thickness with the projected pixel size and integration over the thresholded area results in the total film volume. Multiplying the result with the density of iso-octane of 0.69 mg/mm³ yields the fuel-film mass. Figure 15 shows the decreasing mass of films 1 and 4 with and without combustion. Assuming that the total injected fuel mass of 14 mg splits evenly onto the six single spray cones, each spray cone contains 2.3 mg. Then about 28% of the injected fuel adheres to the wall in the top area, forming film 1 (impingement angle 65°, impingement distance 50 mm). Senda et al. found the adhering fuel fraction to be about 21% at ambient conditions for an impingement distance of 50 mm, an impingement angle of 65°, and an injection pressure of 300 bar [15]. For film 4 (impingement angle 50°, impingement distance 60 mm), only 18 % of the injected mass adheres to the wall. Senda et al. also found the adhering fuel fraction to be about 18 % of the injected fuel for the same impingement. Surprisingly, Figure 15 shows that the evaporation of both fuel films is not affected by combustion. This implies that convective heat transfer from the surrounding gas is negligible compared to the conductive heat transfer from the wall.

This might be explained by the low heat transfer coefficient of about 11 W/(m²·K) between the gas phase and the liquid film. From 3 to 100 ms aSOI the film mass decreases from 0.65 to 0.1 mg for film 1 and from 0.42 to 0 mg for film 4. The film mass has decreased to 60% and 18% of the initial value at 10 ms aSOI for films 1 and 4, respectively. Beyond that time, the film mass decreases nearly linearly in both cases. The high evaporation rate in the beginning might stem from fast heat and mass transfer between the fuel film and the surrounding gas phase due to strong turbulence after injection.

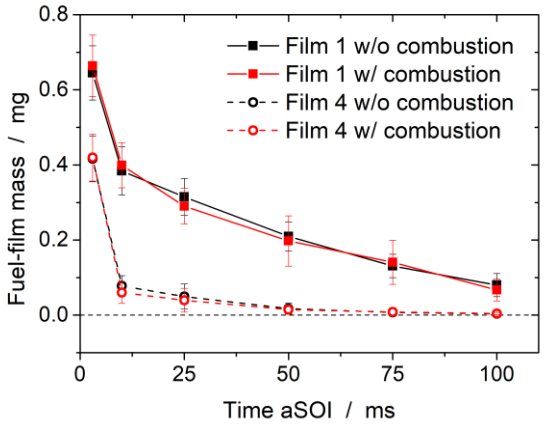

Figure 15: Mass of fuel films 1 and 4 with and without combustion during evaporation. Error bars indicate the standard deviation from 30 (at 3, 25, 75 and 100 ms aSOI) and 70 (at 10 and 50 ms aSOI) individual injections.

Figure 16 shows the temporal evolution of the mean thickness and area of the two films. For both films the area shrinks much more from 3 to 10 ms aSOI than within the following time intervals. The initial areas are very similar with 145 mm² and 150 mm. At 10 ms aSOI 63% and only 15% of the initial film area remain for films 1 and 4, respectively. Beyond that time the fuel-film area decreases approximately linearly in both cases. The initial mean thickness of film 4 of 3.25 µm is significantly lower than the one found for film 1 of 6.25 µm.

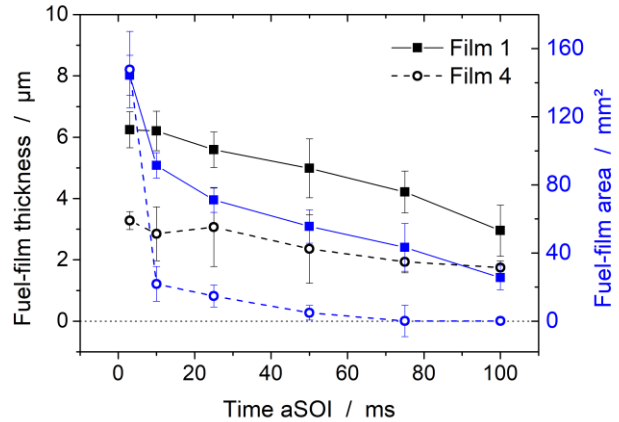

Figure 16: Fuel-film area and thickness of films 1 and 4.

Senda et al. found qualitatively the same trend. The area remained constant for different impingement distances and angles, while the mean film thickness decreased for an increasing impingement distance and decreasing impingement angle [15]. Also, for low-

pressure injection, Cheng et al. found the film area at 3 ms aSOI to be only slightly dependent on the impingement distance. They found that with an injection pressure of 3 bar and an impingement angle of 90°, the film area was 150 and 135 mm² for 50 and 60 mm distance, respectively [16]. The fuel-film thickness decreased nearly linearly for both films during evaporation.

Since the initial area of the two imaged fuel films (1 and 4) is similar at 3 ms aSOI and the boundary conditions for conductive heat transfer from the wall to the liquid are similar, one would expect that similar fractions of the two films have evaporated at 10 ms aSOI. But from Figure 15 it is apparent that from film 4 0.36 and from film 1 0.26 mg evaporate in the first time interval. The explanation is that film 4 is 50% thinner than film 1, leading to a lower heat capacity at 3 ms aSOI. Thus, evaporative cooling lowers the temperature of film 4 more than of film 1. As a consequence, the conductive heat flux from the wall increases due to the increasing temperature gradient, compensating for the evaporative cooling. As a result, a more of film 4 has evaporated at 10 ms aSOI than of film 1.

Figure 17 shows single shots of film 1 in combustion at 10 and 50 ms aSOI for an injection duration of (top) 2.1 and (bottom) 2.6 ms. The corresponding injected masses are 14 and 21 mg (2.3 and 3.5 mg in each spray cone), respectively. Both the fuel-film's thickness and its area are greater than for an injection duration of 2.6 ms. Again, the images for an injection duration of 2.6 ms show an accumulation of fuel into thick droplets at 50 ms aSOI.

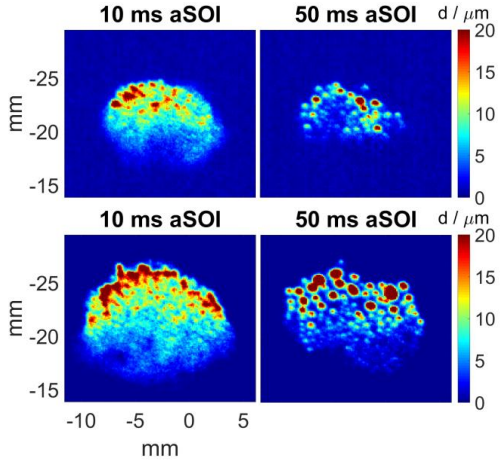

Figure 17: Single shot images of the thickness of film 1 after (top) 2.1 (14 mg) and (bottom) 2.6 ms (21 mg) injection duration with combustion, imaged at 10 and 50 ms aSOI.

Figure 18 compares the mean fuel-film thickness and area for the two injection durations. The initial film area (3 ms aSOI) increases about 71%, while the film thickness increases about 21% for an injection duration of 2.6 ms. This is in good agreement with the results from Senda et al. who found the mean film thickness to be constant at 20 µm when increasing the injection duration from 4 to 8 ms (increasing the injected mass of one spray cone from 7 to 14 mg). At the same time the area increased about 60% when injecting 50% more fuel [15]. This trend changes for very thin films. Maligne et al. investigated fuel films with thicknesses smaller than 1 µm and observed that the film thickness increases about 67% when increasing the injected mass by 50 %. [7]. Figure 18 shows that during most of the evaporation the mean film thickness decreases approximately linearly with a similar slope for both injection durations. Also the fuel-film area decreases with a similar slope in both cases. Only from 3 to 10 ms aSOI the film thickness remains almost constant in both cases. In the same time the area decreases about 28% and 42% for 2.1 and 2.6 ms, respectively. The sharp decrease in the covered area from 3 to 10 ms aSOI corresponds to the complete evaporation of the thin parts seen in the images in Figure 13 and Figure 14 which is why the average thickness (Figure 18) does not change much, despite ongoing evaporation from the entire film.

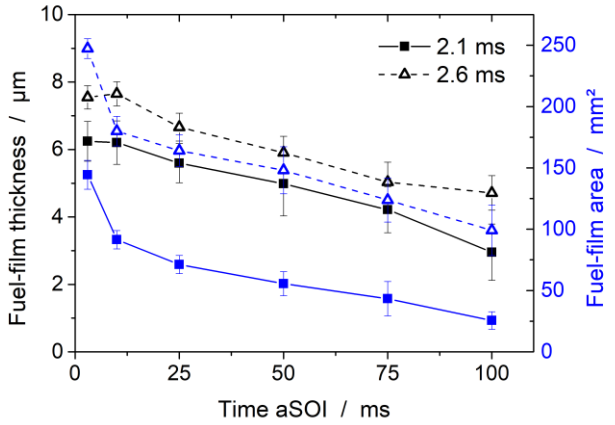

Figure 18: Fuel-film area and thickness of film 1 with combustion for 2.1 and 2.6 ms injection duration.

Figure 19 shows the influence of wall temperature on the evaporation rate of film 1. The data points on each curve are normalized with respect to the film mass at 3 ms aSOI. It should be taken into account that a lower wall temperature leads to a lower air and also injector temperature. The liquid-fuel temperature before start of injection can be approximated by the injector-tip temperature, which is about 5 K below the wall temperature. The investigated wall temperatures are 330, 345, and 365 K. The corresponding air temperatures are 340, 361, and 381 K. Surprisingly, from 3 to 10 ms aSOI the evaporation rate (i.e., the slope of each curve) is similar for the three wall temperatures.

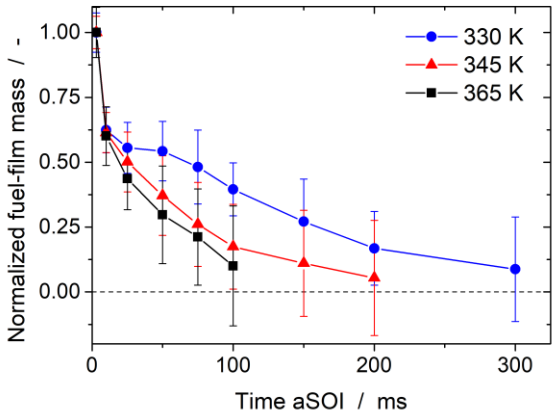

Figure 19: Normalized mass film 1 during evaporation for different quartz-wall temperatures, error bars indicate the standard deviation from 30 (at 3, 25, 75 and 100 ms aSOI) and 70 (at 10 and 50 ms aSOI) individual injections.

This finding is in good agreement with the results of the evaporation curves of films 1 and 4 (see Figure 15), in which the evaporation rate is very high in the first time interval and then approximately constant.

In the first interval, the highly turbulent flow within the tunnel shortly after injection governs the mass transfer from the liquid film into the gas phase. In this interval, a lower wall temperature, and hence film temperature and vapor pressure, do not affect the evaporation rate. After that, the curves in Figure 19 indicate an approximately constant evaporation rate, with the magnitude depending on the particular wall temperature. Now the mass transfer of liquid fuel into the gas phase is determined by the fuel temperature and hence heat-transfer driven. The films have almost completely evaporated at about 100, 200, and 300 ms for wall temperatures of 365, 345, and 330 K, respectively.

Fuel vapor and combustion

Figure 20 shows images of the fuel-vapor distribution in the test section, visualized by LIF (top) and schlieren (bottom). Each LIF image is an ensemble average of 10 single shots. The electrodes and the injector tip are schematically drawn in the top left image. The red dashed line in the second LIF image indicates the field of view for the schlieren imaging. The quartz window that the spray cones impinge on is on the right of the image. Fuel films 1 and 4 are centered at heights of about -20 and 35 mm, respectively, as indicated in the LIF image at 50 ms aSOI.

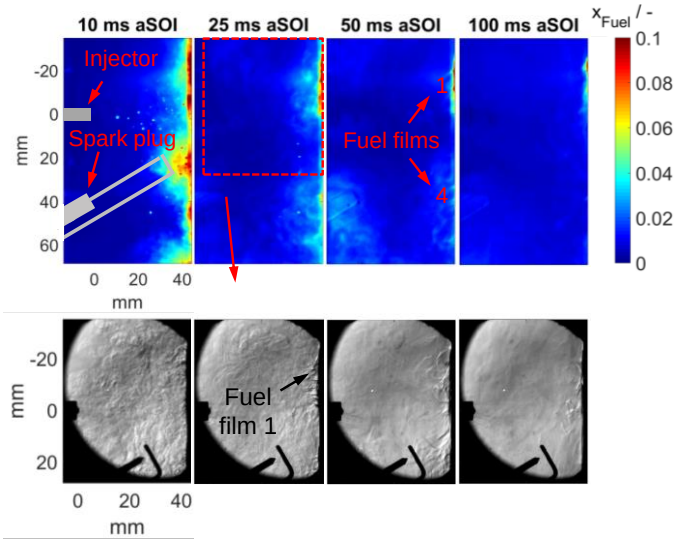

Figure 20: (top) Ensemble averages of the fuel-vapor mole-fraction and (bottom) a corresponding single sequence of schlieren images, both without combustion.

The fuel-rich zone near the electrodes seen at 10 ms aSOI originates from the four spray cones that do almost not impinge on the quartz wall (films 2, 3, 5, and 6). At 25 ms aSOI that zone mostly has been carried out of the light-sheet plane or downstream by the air flow. The detected fuel vapor emerges mainly from films 1 and 4. Schlieren imaging visualizes the density gradients from fuel/air mixing integrated along the line of sight. At 10 ms aSOI the entire field of view is covered by such gradients, indicating the presence of fuel. Also in the schlieren images, the center of film 1 is at a height of about -20 mm. The schlieren images also show that most of the vapor has already been carried out of the field of view (downwards) at 25 ms aSOI. Now the strongest gradients appear close to film 1, indicating its evaporation. At 50 ms aSOI film 4 has almost completely evaporated such that fuel-vapor fluorescence is almost exclusively detected near film 1. The corresponding schlieren image shows the convective transport of the vapor downstream along the wall. The LIF image at 100 ms aSOI shows that film 4 has completely evaporated while fuel still evaporates from the remaining film 1.

Figure 21 shows a schlieren sequence with combustion. The injection, detected by the strong extinction of light by the spray cone, hits the wall and the fuel splashes to the sides and forms film 1.

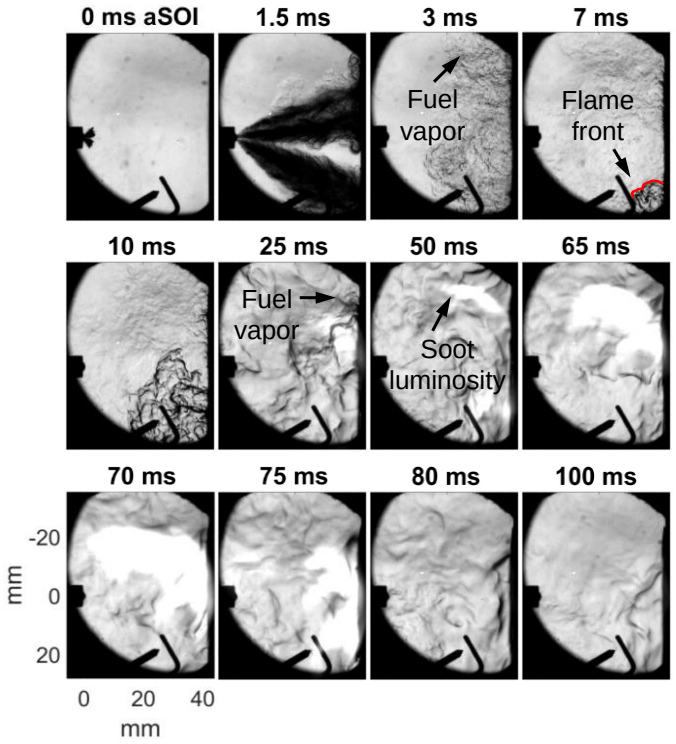

Figure 21: Schlieren images of spray, flame propagation, soot luminosity, and evaporating fuel film.

A weaker intensity gradient can be seen at the edges of the spray cone, indicating the transition to fuel vapor from the liquid. At 3 ms aSOI, the injection has ended and the fuel/air mixture is ignited. Because of the bright schlieren illumination, the spark is not visible. At 7 ms aSOI the flame propagation begins in the lower right corner, where the spark has been convectively transported. The flame front is captured due to strong temperature gradients at the boundary. At 25 ms aSOI the flame has propagated through the test section. The schlieren images show strong gradients close to film 1, which correspond to density and species gradients between burnt gas and fuel vapor. Additionally, natural flame luminosity, presumably soot incandescence, is superimposed on the LED light at 25 and 50 ms aSOI. Hot burnt gas from the main combustion event mixes with surrounding air and newly evaporated fuel from the liquid film, leading to the formation of a sooting flame in this region. Between 65 and 70 ms aSOI, the soot luminosity becomes stronger. Apparently, the flame is fed by fuel vapor, which emerges from the liquid film at the wall in the upper half of the image. The image at 75 ms aSOI indicates that the glowing soot is transported downstream by the flow before its luminosity extinguishes. At 80 ms aSOI the soot luminosity has extinguished. The soot has either cooled down or was transported out of the field of view. Even at 100 ms aSOI, some fuel vapor still emerges from the film but soot formation does not occur. Most probably the gas temperature is now too low to enable pyrolytic formation of PAH.

Figure 22 shows LIF images of the fuel vapor during combustion. Except for the image at 10 ms aSOI, the LIF images are ensemble averages of 10 single shots.

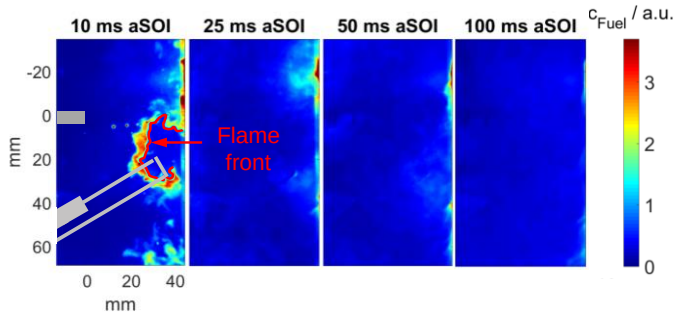

Figure 22: Ensemble averages of the relative fuel-vapor concentration in combustion.

At 10 ms aSOI, the sharply delineated region above the electrode gap corresponds to the burnt gas, in which neither fuel nor tracer are present anymore. Qualitatively, the propagation and position of the flame fronts, visualized by schlieren and LIF at 10 ms aSOI, correlate reasonably well. At 25 ms aSOI the flame has propagated through the test section and again fuel vapor is mainly detected close to the fuel films. A quantification of the fuel-vapor mole-fraction is not possible due to spatially varying temperatures and oxygen partial-pressures.

Soot

Soot formation is investigated by LII and high-speed combustion imaging. For the latter, the high-speed camera was equipped with an orange glass filter (Schott OG 550, 3 mm thickness), transmitting any natural soot incandescence. Figure 23 in the top row shows ensemble averages of 50 LII single shots at different times. In single shots the soot is detected with high spatial intermittency. Below, a sequence of high-speed flame images with the same field of view is shown. The images reveal that soot formation first occurs close to film 4, at 25 ms aSOI. This might be due to higher temperatures in that region since the flame front started to propagate from near there.

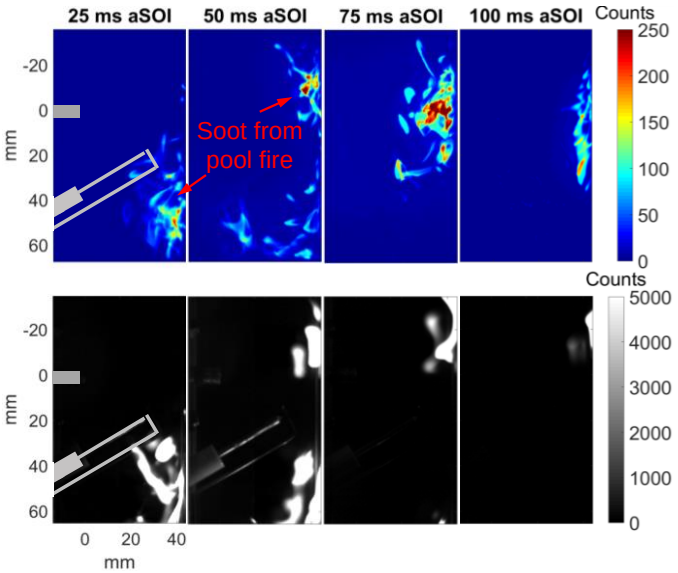

Figure 23: (top) Ensemble averages of soot LII images, (bottom) sequence of high-speed images of natural soot luminosity.

At 50 ms aSOI soot is also detected close to film 1. The high-speed images show sudden soot formation close to film 1 while the schlieren sequence in Figure 21 shows the upstream movement of a sooting flame into the fuel vapor cloud. The LII signal in the lower region decreases either due to oxidation of the soot or due to convective transport downstream out of the field of view. The LII images reveal a large quantity of soot close to film 1 at 75 ms aSOI. This is in good agreement with the sequence of schlieren images in Figure 21, where the maximum extent of the sooting flame is reached at about 70 ms aSOI. It needs to be taken into account that the increase in signal might also stem from the soot of neighboring fuel films (films 2, 3, 5, and 6) that has been transported into the light-sheet plane. At 75 ms aSOI, no soot is detected anymore around film 4 with either imaging technique, which is reasonable since it has evaporated almost completely (see Figure 15). At 100 ms aSOI LII still detects soot along the quartz wall. Apparently, this soot has already cooled down and does not emit natural luminosity anymore but does incandescence after being heated up by the laser-light sheet. The soot is then transported downstream by the flow.

Conclusions and future work

Multiple optical imaging diagnostics were used to investigate the formation of soot from evaporating fuel films in a direct-injection model experiment. The experiment is in the optically accessible test section of a wind tunnel. A GDI injector sprays fuel into the test section. The spray evaporates and mixes with hot air, flowing from top to bottom through the tunnel. Some of the fuel impinges on the quartz wall on the opposite side of the injector and forms fuel films. A pair of electrodes ignites the fuel/air mixture. The flame front propagates through the test section and ignites sooting flames near evaporating fuel films.

The thickness of the fuel films is determined from quantitative tracer LIF imaging. The images show that the films tend to form thick droplets while evaporating from the hot quartz wall. This leads to high spatial intermittency within the fuel-film structure. Also, thin regions with thicknesses between 2 and 4 µm around the fuel film evaporate first, yielding a high evaporation rate shortly after the end of injection and a quick decrease in the fuel film's area. Somewhat surprisingly the results show that the evaporation rate is not influenced by whether the films evaporate in a combusting environment or not. This implies that the convective heat transfer from the surrounding gas phase is negligible compared to the heat flux from the hot wall. In good agreement with the literature, an increase of the injected fuel mass leads more to an increase in the fuel-film area than to an increase in film thickness. In contrast, varying the impingement distance or angle does not influence the wetted area, but the mean film thickness. Therefore, fuel film 4 with a greater impingement distance and angle than fuel film 1 has a similar initial area but 50% lower thickness. In a variation of the wall temperature the evaporation rate shortly after end of injection was not affected by the wall temperature. In this interval, the mass transfer of fuel from the liquid film into the gas phase appears to be governed by the highly turbulent flow near the films. The turbulent flow convectively carries away fuel vapor near the films. After that the evaporation rate is approximately constant and depends on the wall temperature, which also determines the film temperature and hence the vapor pressure.

In a second part of this work the mixing of the gaseous fuel from the films with air is investigated by imaging the fuel-vapor mole fraction. The images show a high concentration of fuel vapor near the liquid

fuel films. Evaporation of fuel into the light-sheet plane is detected until 100 ms aSOI for film 1 and until 75 ms aSOI for film 4. During combustion, schlieren and LIF images both visualize the propagation of the turbulent flame front through the test section, originating from a region close to the electrodes at 10 ms aSOI. At 25 ms aSOI, natural soot luminosity is detected in the schlieren images first near the evaporating film 1. This sooting flame grows up to 70 ms aSOI. The flame extinguishes 75 ms aSOI, even though evaporation from film 1 is still detected. Soot formation stops most probably because the gas phase temperature is too low to enable pyrolytic formation of PAH.

The third part of this work investigates the formation of soot near the evaporating fuel films by means of LII and high-speed images. The results show that soot forms first close to film 4. Since the origin of the flame front lies in this region, higher temperatures than in other regions promote early soot formation. In good agreement, the two diagnostic techniques show that soot formation happens near film 1 at 50 ms aSOI. With further progress in time the LII signal around film 1 becomes stronger, while no signal is detected anymore near film 4, since it has evaporated completely. Results from LII imaging indicate high spatial intermittency in the distribution of soot.

In future work, simultaneous imaging of PAH by LIF, excited at different wavelengths, and soot LII will be done to visualize the transition of fuel vapor to soot precursors and to soot. The quantitative results of the fuel-film thickness and the fuel-vapor mole fraction will serve as validation data for CFD simulations. Currently, a fuel-film evaporation model is being developed and should help to assess heat transfer and its impact on fuel-film evaporation.

References

1. Warey, A., Huang, Y., D. Matthews, R., Hall, M., and Ng, H., "Effects of Piston Wetting on Size and Mass of Particulate Matter Emissions in a DISI Engine," SAE Technical Paper 2002-01-1140, 2002, doi:10.4271/2002-01-1140.
2. Ortmann, R., Arndt, S., Raimann, J., Grzeszik, R., and Würfel, G., "Methods and Analysis of Fuel Injection, Mixture Preparation and Charge Stratification in Different Direct Injected SI Engines," SAE Technical Paper 2001-01-0970, 2001, doi:10.4271/2001-01-0970.
3. Stevens, E., and Steeper, R., "Piston Wetting in an Optical DISI Engine: Fuel Films, Pool Fires, and Soot Generation," SAE Technical Paper 2001-01-1203, 2001, doi:10.4271/2001-01-1203.
4. Drake, M.C., Fansler, T.D., Solomon, A.S., and Szekely, G., "Piston fuel films as a source of smoke and hydrocarbon emissions from a wall-controlled spark-ignited direct-injection engine," SAE Technical Paper 2003-01-0547, 2003, doi:10.4271/2003-01-0547.
5. Stojkovic, B.D., Fansler, T.D., Drake, M.C., and Sick, V., "High-speed imaging of OH* and soot temperature and concentration in a stratified-charge direct-injection gasoline engine," *Proceedings of the Combustion Institute* 30(2):2657-2665, 2005, doi:10.1016/j.proci.2004.08.021.
6. Schulz, F., and Beyrau, F., "Systematic Investigation of Fuel Film Evaporation," SAE Technical Paper 2018-01-0310, 2018, doi:10.4271/2018-01-0310.
7. Maligne, D., and Bruneaux, G., "Time-Resolved Fuel Film Thickness Measurement for Direct Injection SI Engines Using Refractive Index Matching," SAE Technical Paper 2011-01-1215, 2011, doi:10.4271/2011-01-1215.
8. Lin, M.-T., and Sick, V., "Is Toluene a Suitable LIF Tracer for Fuel Film Measurements?," SAE Technical Paper 2004-01-1355, 2004, doi:10.4271/2004-01-1355.
9. Alonso, M., Kay, P.J., Bowen, P.J., Gilchrist, R., and Sapsford, S., "A laser induced fluorescence technique for quantifying transient liquid fuel films utilising total internal reflection," *Experiments in Fluids* 48(1):133-142, 2010, doi:10.1007/s00348-009-0720-8.
10. Kay, P.J., Bowen, P.J., Gold, M., and Sapsford, S. "Development of a 2D quantitative LIF technique towards measurement of transient liquid fuel films," presented at ICLASS-2006, Japan, August 27 - September 1, 2006.
11. Cho, H., and Min, K., "Measurement of liquid fuel film distribution on the cylinder liner of a spark ignition engine using the laser-induced fluorescence technique," *Measurement Science and Technology* 14(7):975-982, 2003, doi:10.1088/0957-0233/14/7/310.
12. Schulz, F., Schmidt, J., and Beyrau, F., "Development of a sensitive experimental set-up for LIF fuel wall film measurements in a pressure vessel," *Experiments in Fluids* 56(5), 2015, doi:10.1007/s00348-015-1971-1.
13. Schulz, F., Samenfink, W., Schmidt, J., and Beyrau, F., "Systematic LIF fuel wall film investigation," *Fuel* 172:284-292, 2016, doi:10.1016/j.fuel.2016.01.017.
14. Zheng, Y., Xie, X., Lai, M.-C., and VanDerWege, B. "Measurement and Simulation of DI Spray Impingements and Film Characteristics," presented at ICLASS 2012, Germany, September 2-6, 2012.
15. Senda, J., Ohnishi, M., Takahashi, T., Fujimoto, H., Utsunomiya, A., and Wakatabe, M., "Measurement and Modeling on Wall Wetted Fuel Film Profile and Mixture Preparation in Intake Port of SI Engine," SAE Technical Paper 1999-01-0798, 1999, doi:10.4271/1999-01-0798.
16. Cheng, Y.-s., Deng, K., and Li, T., "Measurement and simulation of wall-wetted fuel film thickness," *International Journal of Thermal Sciences* 49(4):733-739, 2010, doi:10.1016/j.ijthermalsci.2009.10.006.
17. Almkvist, G., Denbratt, I., Josefsson, G., and Magnusson, I., "Measurements of fuel film thickness in the inlet port of an SI engine by laser induced fluorescence," SAE Technical Paper 952483, 1995, doi:10.4271/952483.
18. Takahashi, Y., Nakase, Y., and Ichinose, H., "Analysis of the Fuel Liquid Film Thickness of a Port Fuel Injection Engine," SAE Technical Paper 2006-01-1051, 2006, doi:10.4271/2006-01-1051.
19. Park, S., and Ghandhi, J.B., "Fuel Film Temperature and Thickness Measurements on the Piston Crown of a Direct-Injection Spark-Ignition Engine," SAE Technical Paper 2005-01-0649, 2005, doi:10.4271/2005-01-0649.
20. Geiler, J.N., Grzeszik, R., Quaing, S., Manz, A., and Kaiser, S.A., "Development of laser-induced fluorescence to quantify in-cylinder fuel wall films," *International Journal of Engine Research* 19(33):134-147, 2018, doi:10.1177/1468087417733865.
21. Schulz, C., and Sick, V., "Tracer-LIF diagnostics: quantitative measurement of fuel concentration, temperature and fuel/air ratio in practical combustion systems," *Progress in Energy and Combustion Science* 31(1):75-121, 2005, doi:10.1016/j.pecs.2004.08.002.
22. Trost, J., Zigan, L., Leipertz, A., Sahoo, D., and C Miles, P., "Characterization of four potential laser-induced fluorescence tracers for diesel engine applications," *Applied*

Optics 52(33):8001-8007, 2013, doi:10.1364/AO.52.008001.
23. Faust, S., Goschütz, M., Kaiser, S., Dreier, T., and Schulz, C., "A comparison of selected organic tracers for quantitative scalar imaging in the gas phase via laser-induced fluorescence," *Applied Physics B* 117(1):183-194, 2014, doi:10.1007/s00340-014-5818-x.
24. Alger, T., Huang, Y., Hall, M., and Matthews, R.D., "Liquid Film Evaporation Off the Piston of a Direct Injection Gasoline Engine," SAE Technical Paper 2001-01-1204, 2001, doi:10.4271/2001-01-1204.
25. Montanaro, A., Allocca, L., Meccariello, G., and Lazzaro, M., "Schlieren and Mie Scattering Imaging System to Evaluate Liquid and Vapor Contours of a Gasoline Spray Impacting on a Heated Wall," SAE Technical Paper 2015-24-2473, 2015, doi:10.4271/2015-24-2473.
26. Montanaro, A., Allocca, L., Lazzaro, M., and Meccariello, G., "Impinging Jets of Fuel on a Heated Surface: Effects of Wall Temperature and Injection Conditions," SAE Technical Paper 2016-01-0863, 2016, doi:10.4271/2016-01-0863.
27. Dec, J.E., zur Loye, A.O., and Siebers, D.L., "Soot Distribution in a D.I. Diesel Engine Using 2-D Laser-Induced Incandescence Imaging," SAE Technical Paper 910224, 1991, doi:10.4271/910224.
28. Dec, J.E.E., Christoph, "Ignition and Early Soot Formation in a DI Diesel Engine Using Multiple 2-D Imaging Diagnostics," SAE Technical Paper 950456, 1995, doi:10.4271/950456.
29. Dec, J.E., "A Conceptual Model of DI Diesel Combustion Based on Laser-Sheet Imaging," SAE Technical Paper 970873, 1997, doi:10.4271/970873.
30. de Francqueville, L.B., G.; Thirouard, B., "Soot Volume Fraction Measurements in a Gasoline Direct Injection Engine by Combined Laser Induced Incandescence and Laser Extinction Method," *SAE Int. J. Engines* 3(1):163-182, 2010, doi:10.4271/2010-01-0346.
31. Hertler, D., Stirn, R., Arndt, S., Grzeszik, R., and Dreizler, A., "Investigations of soot formation in an optically accessible gasoline direct injection engine by means of laser-induced incandescence (LII)," *Applied Physics B* 104(2):399-407, 2011, doi:10.1007/s00340-011-4392-8.
32. Li, J., Matthews, R.D., Stanglmaier, R.H., Roberts, C.E., and Anderson, R.W., "Further Experiments on the Effects of In-Cylinder Wall Wetting on HC Emissions from Direct Injection Gasoline Engines," SAE Technical Paper 1999-01-3661, 1999, doi:10.4271/1999-01-3661.
33. H. Stanglmaier, R., Li, J., and D. Matthews, R., "The Effect of In-Cylinder Wall Wetting Location on the HC Emissions from SI Engines," SAE Technical Paper 1999-01-0502, 1999, doi:10.4271/1999-01-0502.
34. Li, J., Huang, Y., Alger, T., et al., "Liquid Fuel Impingement on In-Cylinder Surfaces as a Source of Hydrocarbon Emissions From Direct Injection Gasoline Engines," *Journal of Engineering for Gas Turbines and Power* 123(3):659-668, 2001, doi:10.1115/1.1370398.
35. Raza, M., Chen, L., Leach, F., and Ding, S., "A Review of Particulate Number (PN) Emissions from Gasoline Direct Injection (GDI) Engines and Their Control Techniques," *Energies* 11(6), 2018, doi:10.3390/en11061417.
36. Robinson, J.W., "Atomic Spectroscopy, Second Edition," (Boca Raton, Taylor & Francis, 1996), 27-28, ISBN: 9780824797423.
37. Zhao, H., "Laser Diagnostics and Optical Measurement Techniques in Internal Combustion Engines," (Warrendale, SAE International, 2012), ISBN: 9780768057829.
38. Goulay, F., Nemes, L., Schrader, P.E., and Michelsen, H.A., "Spontaneous emission from C2(d 3Πg) and C3(A 1Πu) during laser irradiation of soot particles," *Molecular Physics* 108(7-9):1013-1025, 2010, doi:10.1080/00268971003627824.
39. Berlman, I.B., "Handbook of Fluorescence Spectra of Aromatic Molecules, Second Edition," (New York and London, Academic Press, 1971), 113-115, ISBN: 9780323161671.
40. Semrock, "Transmission spectrum of 292/27 nm single-band bandpass filter," https://www.semrock.com/filterdetails.aspx?id=ff01-292/27-25, accessed Sept. 2018
41. Semrock, "Transmission spectrum of 266 nm ultrasteep long-pass edge filter," https://www.semrock.com/filterdetails.aspx?id=lp02-266ru-25, accessed Sept. 2018
42. Faust, S.M., "Characterisation of organic fuel tracers for laser-based quantitative diagnostics of fuel concentration, temperature, and equivalence ratio in practical combustion processes", Dissertation, Mechanical and Process Engineering Department, University of Duisburg-Essen, Duisburg, 2013.
43. Ramart-Lucas, M., and Bertucat, S., "Déformation de la structure électronique du carbone par effet stérique (Série de la pyridine)," *Bulletin De La Societe Chimique De France* 18:212-214, 1951.
44. Benzler, T., Endres, T., Dreier, T., and Schulz, C., "Temperature, pressure, and oxygen quenching behavior of fluorescence spectra and lifetimes of gas-phase o-xylene and 1,2,4-trimethylbenzene," *Applied Physics B* 124(4):70, 2018, doi:10.1007/s00340-018-6937-6.

Contact Information

Sebastian Kaiser
University of Duisburg-Essen
Institute for Combustion and Gas Dynamics (IVG)
sebastian.kaiser@uni-due.de

Acknowledgments

The work reported in this publication has been undertaken as part of the PaREGEn (Particle Reduced, Efficient Gasoline Engines) project. This project has received funding from the European Union's Horizon2020 Programme for research and technology development and demonstration under grant agreement no. 723954. We thank Bosch for hardware support and in particular J. Geiler at Bosch and Daniel Fuhrmann at the University of Duisburg-Essen for fruitful discussions on fuel-film imaging.